Soils, granular media, civil engineering

Bifurcations in granular media: macro- and micro-mechanics approaches

Félix Darve [a,*], Luc Sibille [a], Ali Daouadji [b], François Nicot [c]

[a] *Laboratoire sols solides structures, UJF–INPG–CNRS, 38041 Grenoble, France*
[b] *Laboratoire de physique et mécanique des matériaux, UPV-M, CNRS, Metz, France*
[c] *Cemagref, Unité de Recherche Erosion torrentielle neige et avalanches, Grenoble, France*

Abstract

Various failure modes related to different kinds of bifurcations occur in nonassociated elastoplastic materials such as geomaterials. After presenting experimental evidence, we study this question by means of phenomenological constitutive relations and direct numerical simulations based on the discrete element method. The second-order work criterion related to diffuse failure modes is particularly considered within the framework of continuum and discrete mechanics. The equations of the bifurcation domain boundary and unstable stress direction cones are established. Diffuse failure is simulated numerically by perturbing bifurcation states. *To cite this article: F. Darve et al., C. R. Mecanique 335 (2007).*
© 2007 Académie des sciences. Published by Elsevier Masson SAS. All rights reserved.

Résumé

Bifurcations dans les milieux granulaires : approches macro- et micro-mécaniques. Différents modes de rupture reliés à différents types de bifurcations apparaissent dans des matériaux élasto-plastiques non-associés tels que les géomatériaux. Après avoir présenté quelques résultats expérimentaux typiques, cette question est abordée au moyen de relations constitutives phénoménologiques et de simulations numériques directes basées sur la méthode des éléments discrets. Le critère du travail du second ordre lié aux modes de rupture diffuse est particulièrement étudié dans le cadre de la mécanique des milieux continus et des milieux discrets. Les équations des limites du domaine de bifurcation et des cônes de directions de contrainte instables sont établies. La rupture diffuse est simulée numériquement par des perturbations des états de bifurcation. *Pour citer cet article : F. Darve et al., C. R. Mecanique 335 (2007).*
© 2007 Académie des sciences. Published by Elsevier Masson SAS. All rights reserved.

* Corresponding author.

E-mail addresses: Felix.Darve@inpg.fr (F. Darve), luc.sibille@univ-nantes.fr (L. Sibille), ali.daouadji@univ-metz.fr (A. Daouadji), francois.nicot@grenoble.cemagref.fr (F. Nicot).

1. Introduction

Geomechanics is traditionally divided into two major parts: foundation settlements and the problems of failure in geotechnical engineering. The first is based on elastic analyses using Hooke's law for the soil, while the second is based on the Mohr–Coulomb plastic criterion. Indeed, the development of elastoplastic finite element computations were a necessary prerequisite to obtaining a unified geomechanics corpus.

It is remarkable that the elastic computations in soil and rock mechanics are essentially based on Boussinesq's formula (Boussinesq [1]), expressing the vertical stress field in a homogeneous isotropic linear elastic half space subjected to a vertical force on the free surface. In a rather strange way, it appears that these vertical stresses are independent of any mechanical property (i.e., neither Young's modulus nor Poisson's ratio). The beauty and the success of Boussinesq's formula are probably due to this direct simplicity. The so-called oedometric modulus (measured in the laboratory) can be used to deduce the vertical strains, which by vertical integration give the settlements of the free surface below the applied foundation. Before the developments of the finite element method, it was the only way to estimate the settlements of a building or an embankment. The first author of this paper carried out his first research project (Darve [2]) on a specific analytical 3D integration of Boussinesq's formula.

Today advanced geomechanics (in addition to the development of finite element computations with proper constitutive relations for soils and rocks) means taking into account bifurcation criteria to describe the various modes of failure (localized, diffuse, etc.) that occur in geomaterials as a result of the recent successes in the micro-mechanics of granular media (which were called 'milieux pulvérulents' by J. Boussinesq [3]). This paper explores the question of diffuse failure in granular materials using three different approaches: phenomenological incrementally nonlinear constitutive relations, micro-mechanical models and discrete element simulations.

First of all, what is diffuse failure? This notion was introduced in geomechanics in 1998 (Darve and Roguiez [4]) to describe failure modes with no strain localization pattern in either shear bands or compaction/dilation bands. In the second section of this paper, drained and undrained triaxial experimental results are presented and discussed to characterise this type of failure on clear experimental bases.

While localized failure is described by the vanishing values of the determinant of the acoustic tensor (Rice [5]), it has been conjectured and experimentally validated (Darve and Chau [6], Nova [7], Darve and Laouafa [8], Darve et al. [9], Khoa et al. [10]) that the second-order work criterion (Hill [11], Mandel [12]) could be a proper indicator of diffuse failure. This criterion is presented in Section 3. Its physical meaning in terms of leading to unstable behaviours is discussed. The link between the second-order work at the macroscopic scale (i.e. the specimen) and the microscopic level (i.e. the grains) is explained. Dynamic effects through bursts of kinetic energy are emphasised.

The fourth section is then devoted to the application of this criterion to sands whose mechanical behaviour is described by incrementally piece-wise linear and nonlinear constitutive relations. Bifurcation domains and cones of unstable stress directions are determined analytically and numerically.

Finally, in the fifth section, a discrete element model (Magnier and Donzé [13]) is used to compute macro- and micro-values of second-order work in a specimen of spherical particles. The analytical relations of Section 3 are numerically treated and diffuse failure modes are simulated and analysed.

2. Experimental analysis of instabilities in very loose sands

This section describes the modes of failure at the bifurcation state. A new test is proposed to apply a particular path: a quasi constant shear stress undrained test (CSU). This type of loading program has the advantage of checking whether excess pore pressure is the consequence of collapse, as was shown by Eckersley [14] for drained tests. In other words, is excess pore pressure a trigger parameter under undrained conditions?

It will be established that collapse can occur inside a domain which is included in the Mohr–Coulomb limit surface and that collapse depends on the direction of the loading (Darve et al. [9]). A definition of an unstable domain is proposed for undrained compression triaxial tests (ICU), for constant shear drained tests (CSD) and for constant shear undrained tests (CSU). All tests are isotropically consolidated.

2.1. Experimental setup

An experimental arrangement was developed to impose a constant shear stress on the soil specimen. Unlike in previous experimental studies on dry sand (Skopek et al. [15]) and drained saturated sands (Sasitharan et al. [16],
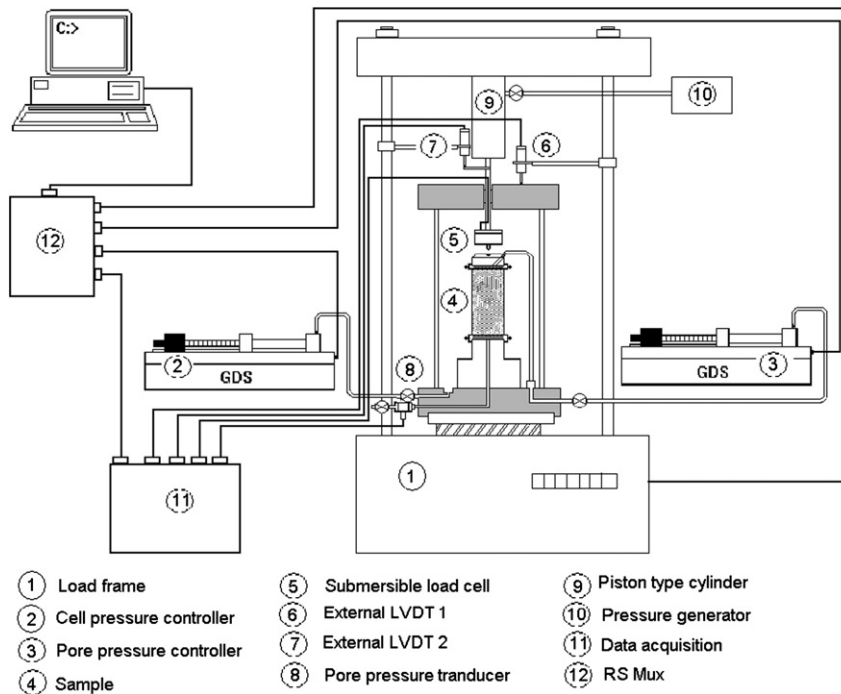
Fig. 1. Testing arrangement.

Fig. 1. Dispositif expérimental.

di Prisco and Imposimato [17], Gajo [18]) this particular loading path (detailed in Section 2.3) is applied under undrained conditions. First, the components of the entire experimental setup will be briefly presented and then the testing procedure and the characteristics of the tested sand will be described.

Axial displacement is imposed by a displacement-controlled loading frame. The displacement rate is chosen by selecting a velocity in the range of 0.00001 to 5.99999 mm/min. However, the loading can be completely applied via a piston-type cylinder which is assembled on the apparatus. So mixed loading (i.e. displacement-controlled then load-controlled) can be applied. Two digital pressure/volume controllers (DPVC) are used to perform isotropic consolidated drained tests. Back pressure is measured with a pore pressure transducer. During testing, the measured value is compared to the applied pressure in order to verify that the strain or the stress rate is not too high. Axial displacement is measured by an external LVDT and volume changes by the piston displacement into and out of the DPVC. The forces are measured by an internal submersible load cell. All test variables are stored in a microcomputer. A schematic presentation is given in Fig. 1.

2.2. Tested material and sample preparation

The sand used for this study is Hostun S28 sand. The quartzic grains are subangular and the grain size distribution is uniform. The principal characteristics are summarised in Table 1. The moist tamping (MT) method was used to prepare the specimen. The sand had a moisture content of approximately 3–4% in order to reach the maximal void ratio before and after isotropic consolidation (Table 1). In order to obtain homogeneous samples, sand was carefully placed in five layers in the mould. During the saturation process, the B-Skempton coefficient was checked and samples were assumed to be saturated if $B \geqslant 96\%$.

2.3. Testing program

For a given void ratio, three effective mean pressures were applied: $p'_o = 100$, 300 and 750 kPa. The first series of tests concern undrained triaxial tests, the second series is constant shear drained tests, and the third series is quasi-constant shear undrained tests.

Table 1
Basic properties of Hostun S28 sand

Tableau 1
Propriétés du sable d'Hostun S28

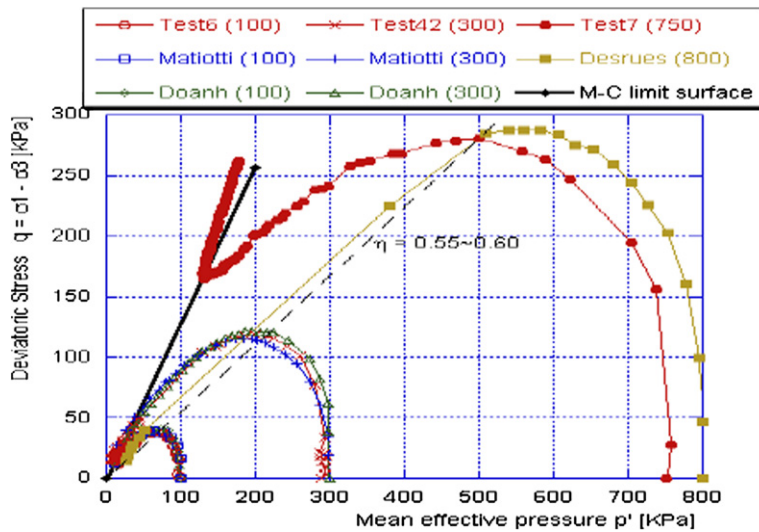| Type	Mean Size (mm)	Uniformity coefficient	Specific gravity	Max void ratio	Min void ratio	Frictional angle (°)
Quartzic	0.3–0.35	2	2.65	1	0.656	32

Fig. 2. Comparison of our results with those of Matiotti et al. [19], Doanh et al. [20] and Servant et al. [21] for $p'_o = 100, 300, 750$ kPa.

Fig. 2. Comparaison entre nos résultats et ceux obtenus par Matiotti et al. [19], Doanh et al. [20] et Servant et al. [21], pour $p'_o = 100, 300, 750$ kPa.

2.3.1. Isotropically consolidated undrained compression tests

The results obtained for load-controlled tests are compared to those obtained by Matiotti et al. [19], Doanh et al. [20] and described by Servant et al. [21] and Khoa et al. [10] for displacement-controlled tests on same sand with a very close density. The experimental device described by Servant et al. [21] and Khoa et al. [10] is a displacement-controlled device which was modified so that a constant stiffness could be applied at peak shear stress. The constant stiffness results from a spring attached to the displacement-controlled device. At the peak of stress, it is noted that $\eta = q/p'$ is equal to 0.6, which corresponds to a mobilised angle of friction of approximately 16°. Good agreement is shown for all these experimental results in Fig. 2.

2.3.2. Constant shear drained (CSD) tests

This test was originally developed by Sasitharan et al. [16] on saturated loose Ottawa sand sheared under drained conditions with dead load. This special stress path was performed to simulate the loading of soil within a slope or an embankment subjected to a low increase in pore pressure. Di Prisco and Imposimato [17] and Gajo [18] conducted similar tests on Hostun sand for approximately the same void ratio as in our experiments. The constant shear stress is also applied using dead load. Fig. 3 presents the main results, obtained either by increasing the pore pressure (tests # 58 and 61) or by decreasing total stresses (tests # 51 and 60).

2.3.3. Constant shear undrained tests

In the case of a sudden increase in pore pressure (heavy rainfall, for example), assuming that the material behaves under drained conditions is no longer valid. A quasi-constant shear undrained test (CSU) is proposed to simulate, in a more realistic way, the in situ conditions with a constant load and a rapid increase in pore pressure. After a shearing phase, the shear stress is kept quasi-constant by decreasing total stresses and by closing the drainage valve (Fig. 4).
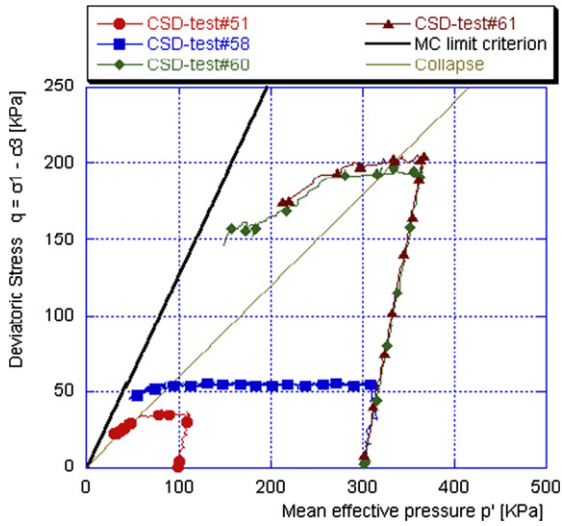
Fig. 3. Constant shear drained tests on Hostun sand.

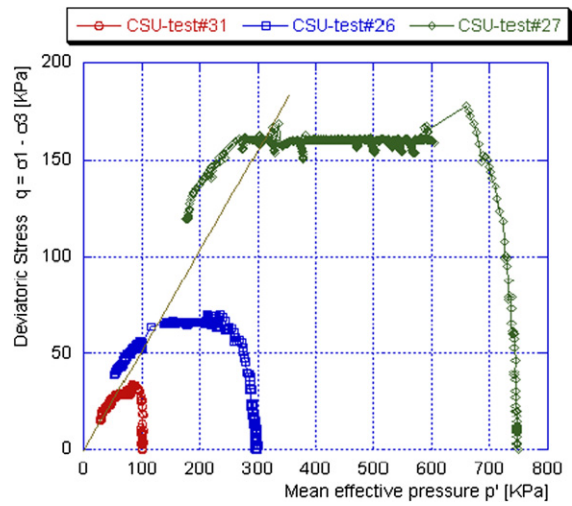Fig. 3. Essais drainés à cisaillement constant sur un sable d'Hostun.

Fig. 4. Constant shear undrained tests on Hostun sand.

Fig. 4. Essais non drainés à cisaillement constant sur un sable d'Hostun.

Table 2
Mobilised angles of friction and stress ratios for ICU, CSD and CSU tests

Tableau 2
Angles de frottement mobilisés et rapports de contraintes pour les essais ICU, CSD et CSU

Type of test	Test #	p'_0 (KPa)	e_o	ϕ_{mob} (°)	$(q/p')_{\mathrm{coll}}$
ICU	6	100	1.086	15.26	0.58
	42	300	1.060	15.67	0.59
	7	750	1.083	14.89	0.56
CSD	51	100	1.192	15.06	0.57
	58	300	1.068	14.49	0.55
	60	300	1.161	16.53	0.62
CSU	31	100	1.136	13.91	0.52
	26	300	1.070	14.72	0.56
	41	300	1.101	13.64	0.51
	27	750	1.136	15.36	0.58

2.4. Experimental evidence

Experimental collapse points obtained from ICU, CSD and CSU tests are plotted in Fig. 5. Collapse means here that the sample is no longer controllable (Nova [22]). The loading program, with the chosen control parameters, cannot be maintained. One can see that the stress ratios and the corresponding mobilised angles of friction at collapse are very close (Table 2). It is relevant to note that collapse occurs strictly within a domain which is included in the Mohr–Coulomb limit surface. Taking into account experimental uncertainties, the unstable line seems to be unique for all the loading paths considered. This result is of course not generally valid and here could be due to the fact that, at collapse, stress increments are parallel, as depicted in Fig. 7.

The deformation of all the samples seems to be homogeneous even for large strains (after collapse): we note no strain localisation either by a single shear band or by a shear band pattern. The analysis of pore pressure variation at collapse on Fig. 6 highlights two points:

– Collapse occurs while the pore pressure decreases, meaning that the increase in pore pressure is related to collapse itself (Fig. 6(a)), as pointed out also by Imposimato and Nova [23];
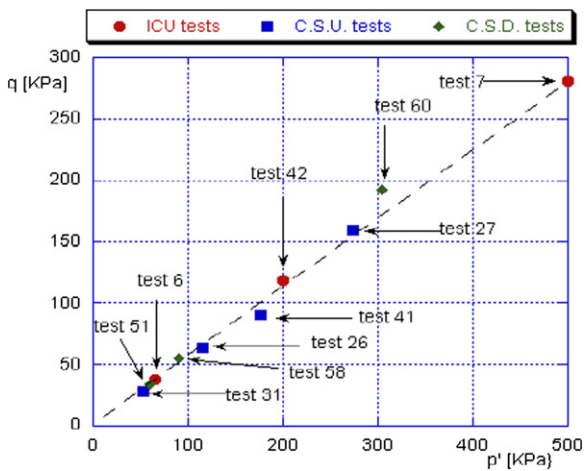
Fig. 5. Collapse points for ICU, CSD and CSU tests.

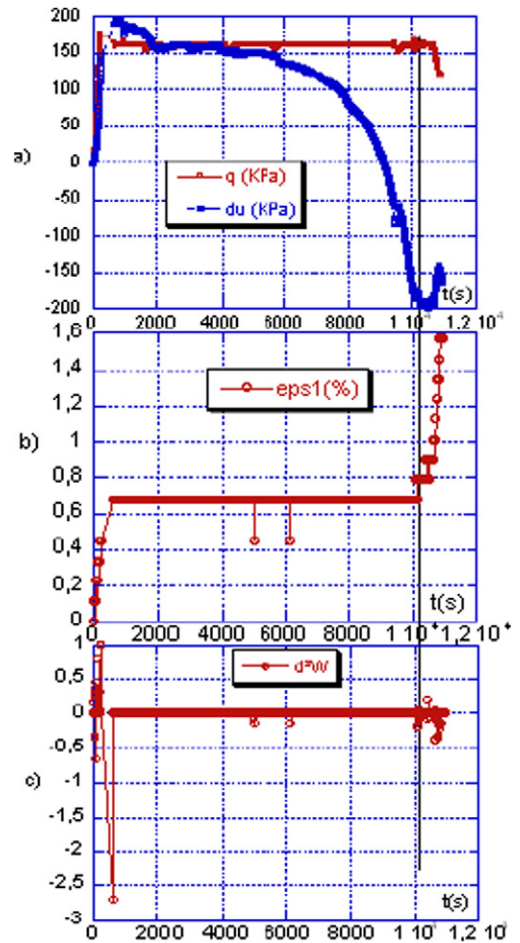Fig. 5. Points d'effondrement pour les essais ICU, CSD et CSU.

Fig. 6. Changes in shear stress and variation in pore pressure (a), axial displacement (b) and second-order work (c) versus time (CSU).

Fig. 6. Evolutions de la contrainte de cisaillement et de la pression interstitielle (a), de la déformation axiale (b) et du travail du second ordre (c), en fonction du temps (CSU).

– The increase in pore pressure during collapse is more than likely the result of a diffuse mode of deformation rather than a localised one since, upon localised deformation, no notable change in pore pressure should be observed. This diffuse mode of failure will be analysed in Sections 3 and 4.

The collapses (or instabilities) detected experimentally in this section correspond more generally to bifurcation states. Therefore, the next section investigates the collapse of a material point or a homogeneous sample in the general context of bifurcation (Petrik [24], Bigoni [25]). A criterion is built to detect the occurrence of such collapses, and finally this notion is applied to the case of a granular assembly.

3. The second-order work as a bifurcation criterion

In this section, it is established that a mechanical system, in equilibrium under prescribed boundary conditions, may develop kinetic energy with no change in the control parameters governing the boundary conditions. As a bifurcation corresponds to a sudden change in the state of a system under continuous variations in the state variables, the development of kinetic energy is a proper bifurcation mode. The vanishing of the second-order work, as defined by
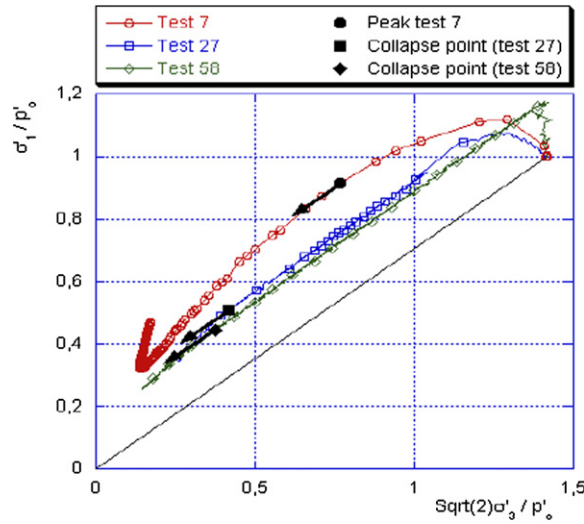
Fig. 7. Orientation of stress increments for ICU, CSD and CSU tests.

Fig. 7. Orientation de l'incrément de contrainte pour les essais ICU, CSD et CSU.

Hill [11], is shown to play a fundamental role in detecting whether a mechanical state of a given system corresponds to such a bifurcation.

A system made up of a volume V_o of a given material, initially in a configuration C_o (the position of a material point is denoted $\vec{X}$ in this initial configuration) is considered. After a loading history, the system is in a strained configuration C and occupies a volume V, in equilibrium under a prescribed external loading (the position of a material point is denoted $\vec{x}$ in this current configuration). This loading is controlled by specific static or kinematic parameters, referred to as the control parameters.

3.1. Loss of sustainability of a mechanical state: a bifurcation point

Let a volume of a rate-independent material, defined by both stress $\bar{\bar{\sigma}}$ and displacement $\vec{u}$ fields, be in equilibrium under a loading governed by specific control parameters. The mechanical state of the system is reputed unsustainable if and only if two related incremental displacement and stress fields $\delta\vec{u}$ and $\delta\bar{\bar{\sigma}}$ exist, such that $\bar{\bar{L}}\delta t$ (where $L_{ij}\delta t = \frac{\partial(\delta u_i)}{\partial x_j}$ is the component of the velocity gradient tensor $\bar{\bar{L}}$) and $\delta\bar{\bar{\sigma}}$ are related by the constitutive relation, and such that the state (which is not necessarily in equilibrium) defined by both stress $\bar{\bar{\sigma}} + \delta\bar{\bar{\sigma}}$ and displacement $\vec{u} + \delta\vec{u}$ fields can be encountered by the system with no changes in the control parameters. In this case, kinetic energy is created from an equilibrium state with no change in the control parameters. This is therefore a proper bifurcation state.

3.2. Loss of sustainability and vanishing of the second-order work

The instantaneous change in the system, in the equilibrium configuration C at time t, is governed by the following energy conservation equation:

$$\delta E_c(t) = \int_{\Gamma} f_i \delta u_i \, \mathrm{d}S - \int_{V} \sigma_{ij} \frac{\partial(\delta u_i)}{\partial x_j} \, \mathrm{d}V \tag{1}$$

where δE_c represents the current change in kinetic energy of the system and $\vec{f}\,\mathrm{d}S$ is the current external force acting on the current boundary of the system. It is convenient to express the integrals in Eq. (1) with respect to the initial configuration, which yields:

$$\delta E_c(t) = \int_{\Gamma_o} F_i \delta u_i \, \mathrm{d}S_o - \int_{V_o} \Pi_{ij} \frac{\partial(\delta u_i)}{\partial X_j} \, \mathrm{d}V_o \tag{2}$$

where $\overline{\overline{\Pi}}$ denotes the Piola–Kirchoff stress tensor of the first kind, Γ_o is the V_o boundary, and $\vec{F}\,\mathrm{d}S_o$ is the current external force acting on the boundary of the system in the initial configuration. Differentiation of Eq. (2) gives:

$$\delta^2 E_c(t) = \int_{\Gamma_o} \delta F_i \delta u_i \,\mathrm{d}S_o + \int_{\Gamma_o} F_i \delta^2 u_i \,\mathrm{d}S_o - \int_{V_o} \delta \Pi_{ij} \frac{\partial(\delta u_i)}{\partial X_j} \,\mathrm{d}V_o - \int_{V_o} \Pi_{ij} \frac{\partial(\delta^2 u_i)}{\partial X_j} \,\mathrm{d}V_o \tag{3}$$

By taking advantage of Green's formula, Eq. (3) yields:

$$\delta^2 E_c(t) = \int_{\Gamma_o} \delta F_i \delta u_i \,\mathrm{d}S_o - \int_{V_o} \delta \Pi_{ij} \frac{\partial(\delta u_i)}{\partial X_j} \,\mathrm{d}V_o \tag{4}$$

The system is controlled either by the external force density $\vec{F}$, or by the boundary displacement $\vec{u}$. Imposing that the control parameters do not change implies that $\int_{\Gamma_o} \delta F_i \delta u_i \,\mathrm{d}S_o = 0$. In ignoring third-order terms, then $\delta^2 E_c(t) = 2E_c(t + \delta t)$, and it follows:

$$2E_c(t + \delta t) = - \int_{V_o} \delta \Pi_{ij} \left(\frac{\partial(\delta u_i)}{\partial X_j} \right) \mathrm{d}V_o \tag{5}$$

Eq. (5) represents the rate expression of the system's energy conservation from an equilibrium state. It must be emphasised that Eq. (5) no longer applies once the system is off-equilibrium. As $E_c(t + \delta t) > 0$, the system evolves toward another mechanical state if and only if:

$$\int_{V_o} \delta \Pi_{ij} \left(\frac{\partial(\delta u_i)}{\partial X_j} \right) \mathrm{d}V_o < 0 \tag{6}$$

Defining the second-order work as the quantity:

$$W_2 = \int_{V_o} \delta \Pi_{ij} \left(\frac{\partial(\delta u_i)}{\partial X_j} \right) \mathrm{d}V_o \tag{7}$$

expressed through a semi-Lagrangian formalism, the system evolves from the equilibrium configuration C toward another mechanical state if and only if:

$$W_2 < 0 \tag{8}$$

An Eulerian expression of the second-order work can be given by making use of the Piola transform of the Cauchy stress tensor. As $\delta \overline{\overline{\Pi}} = J(\delta \overline{\overline{\sigma}} + J \operatorname{div}(\delta \vec{u}) \overline{\overline{\sigma}} - \overline{\overline{\sigma}}(\overline{\overline{L}})^t \delta t)(\overline{\overline{F}}^{-1})^t$, then, by combining with Eq. (7), it follows that:

$$W_2 = \int_V \left(\delta \overline{\overline{\sigma}} + \operatorname{div}(\delta \vec{u}) \overline{\overline{\sigma}} - \overline{\overline{\sigma}}(\overline{\overline{L}})^t \delta t \right) : \overline{\overline{L}} \delta t \,\mathrm{d}V \tag{9}$$

For a material point or a homogeneous specimen (according to the meaning of continuum mechanics), Eq. (9) reads:

$$W_2 = V \left(\delta \overline{\overline{\sigma}} + \operatorname{div}(\delta \vec{u}) \overline{\overline{\sigma}} - \overline{\overline{\sigma}}(\overline{\overline{L}})^t \delta t \right) : \overline{\overline{L}} \delta t \tag{10}$$

The second-order work is thus a combination of three terms, namely $V \delta \overline{\overline{\sigma}} : \overline{\overline{L}} \delta t$, $V \operatorname{div}(\delta \vec{u}) \overline{\overline{\sigma}} : \overline{\overline{L}} \delta t$, and $-V \overline{\overline{\sigma}}(\overline{\overline{L}})^t \delta t : \overline{\overline{L}} \delta t$, which will be investigated from discrete numerical simulations in Section 5.

3.3. Application to the case of granular materials

A granular assembly composed of N grains 'p', with $1 \leqslant p \leqslant N$, is considered (Fig. 8). The mass center of each grain 'p' is denoted G_p. Each grain 'p' is in contact with n_p other grains 'q'. The set of grains 'q' in contact with grain 'p' is defined by the mapping $q = C_p(k)$, with $k = 1, \ldots, n_p$. Whatever p is, n_p is nonzero. Each grain 'p' belonging to the boundary ∂V of the volume is subjected to an external force $\vec{F}^{\mathrm{ext},p}$. It will be assumed that no torque is applied to the particles of ∂V: $\forall p \in \partial V,\ \delta \vec{M}^{\mathrm{ext},p} = \vec{0}$.
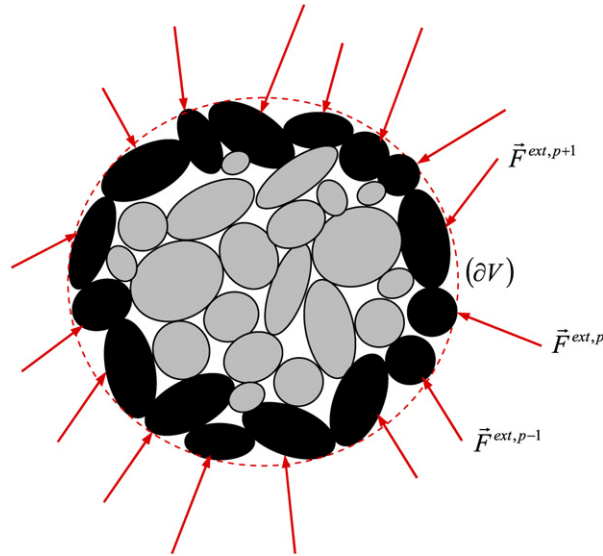
Fig. 8. Definition of the granular assembly. Boundary of the volume and external forces.

Fig. 8. Définition de l'assemblage granulaire. Frontière du volume et forces externes.
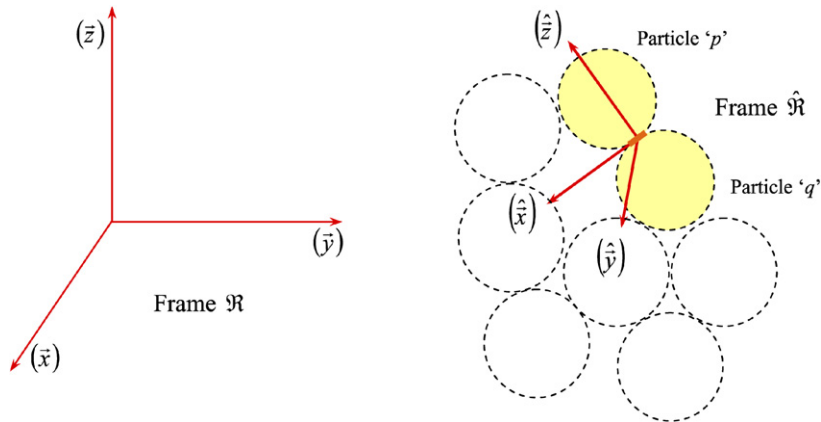

Fig. 9. Definition of both the Galilean reference frame and the local frame attached to two contacting granules.

Fig. 9. Définition du repère galiléen de référence, et du repère local lié à deux grains en contact.

Let two particles 'p' and 'q' of the granular assembly be in contact. Let $\Re$ be a Galilean frame. The local frame $\hat{\Re}\{\hat{\bar{x}}, \hat{\bar{y}}, \hat{\bar{z}}\}$ attached to the contact considered is introduced, where $\hat{\bar{z}}$ is normal to the tangent plane, and $\hat{\bar{x}}$ and $\hat{\bar{y}}$ belong to the tangent plane so that $\{\hat{\bar{x}}, \hat{\bar{y}}, \hat{\bar{z}}\}$ defines a direct triad (Fig. 9). The time differentiation of any variable ψ with respect to this frame will be denoted $\hat{\delta}\psi$.

Let $\hat{\delta}\vec{u}_c^{p,q}$ define the relative displacement of particle 'p' with respect to particle 'q', and $\hat{\delta}\vec{F}^{p,q}$ the contact force applied by particle 'p' onto particle 'q'. It can be shown that the second-order work associated with the two contacting granules 'p' and 'q' can be expressed from discrete variables as follows (Nicot and Darve [26]):

$$W_2^{p,q} = \hat{\delta}\vec{F}^{p,q} \cdot \hat{\delta}\vec{u}_c^{p,q} \tag{11}$$

Furthermore, starting from an equilibrium state, the rate formulation of the energy conservation reads:

$$W_2 = \sum_{p \in \partial V} \delta\vec{F}^{\text{ext},p} \cdot \delta\vec{u}^p - \delta^2 E_c(t) \tag{12}$$

However, incremental kinetic energy of the granular assembly considered reads:

$$\delta E_c(t) = \sum_{p=1}^{N} \left(\vec{F}^p \cdot \delta \vec{u}^p + \vec{M}^p \cdot \delta \vec{\omega}^p \right) \tag{13}$$

where $\vec{F}^p$ and $\vec{M}^p$ are the external force and the external torque, respectively, exerted on any particle 'p' considered. The incremental changes $\delta \vec{F}^p$ and $\delta \vec{M}^p$ are linked to an incremental displacement $\delta \vec{u}^p$ and to an incremental rotation $\delta \vec{\omega}^p$ of particle 'p'. After differentiation, Eq. (13) yields:

$$\delta^2 E_c(t) = \sum_{p=1}^{N} \left(\vec{F}^p \cdot \delta^2 \vec{u}^p + \vec{M}^p \cdot \delta^2 \vec{\omega}^p + \delta \vec{F}^p \cdot \delta \vec{u}^p + \delta \vec{M}^p \cdot \delta \vec{\omega}^p \right) \tag{14}$$

As $\vec{F}^p = \sum_{k=1}^{n_p} \vec{F}^{C_p(k),p} + \vec{F}^{\text{ext},p}$ and $\vec{M}^p = \sum_{k=1}^{n_p} (\overrightarrow{G_p C_p^k} \wedge \vec{F}^{C_p(k),p})$, where $\vec{F}^{C_p(k),p}$ represents the force applied by particle '$C_p(k)$' onto particle 'p' at the contact point C_p^k, and $\vec{F}^{\text{ext},p}$ is the external force applied to particle 'p', excluding contact forces; it follows after differentiation:

$$\delta \vec{F}^p = \sum_{k=1}^{n_p(t+\delta t)} \delta \vec{F}^{C_p(k),p} + \delta \vec{F}^{\text{ext},p} \tag{15}$$

and:

$$\delta \vec{M}^p = \sum_{k=1}^{n_p(t+\delta t)} \left(\overrightarrow{G_p C_p^k} \wedge \delta \vec{F}^{C_p(k),p} + \delta \left(\overrightarrow{G_p C_p^k} \right) \wedge \vec{F}^{C_p(k),p} \right) + \delta \vec{M}^{\text{ext},p} \tag{16}$$

Hence, it can be written that:

$$\sum_{p=1}^{N} \left(\delta \vec{F}^p \cdot \delta \vec{u}^p + \delta \vec{M}^p \cdot \delta \vec{\omega}^p \right) = \sum_{p=1}^{N} \sum_{q=1}^{N} \left(\delta \vec{F}^{q,p} \cdot \left(\delta \vec{u}^p - \overrightarrow{G_p C_{p,q}} \wedge \delta \vec{\omega}^p \right) - \vec{F}^{q,p} \cdot \delta \left(\overrightarrow{G_p C_{p,q}} \right) \wedge \delta \vec{\omega}^p \right) + \cdots$$
$$+ \sum_{p \in \partial V} \left(\delta \vec{F}^{\text{ext},p} \cdot \delta \vec{u}^p \right) \tag{17}$$

Likewise, we have:

$$\sum_{p=1}^{N} \left(\vec{F}^p \cdot \delta^2 \vec{u}^p + \vec{M}^p \cdot \delta^2 \vec{\omega}^p \right) = \sum_{p=1}^{N} \sum_{q=1}^{N} \left(\vec{F}^{q,p} \cdot \left(\delta^2 \vec{u}^p - \overrightarrow{G_p C_{p,q}} \wedge \delta^2 \vec{\omega}^p \right) \right) + \sum_{p \in \partial V} \left(\vec{F}^{\text{ext},p} \cdot \delta^2 \vec{u}^p \right) \tag{18}$$

It follows that:

$$\delta^2 E_c(t) = \sum_{p=1}^{N} \sum_{q=1}^{N} \left(\delta \vec{F}^{q,p} \cdot \left(\delta \vec{u}^p - \vec{r}^{p,q} \wedge \delta \vec{\omega}^p \right) + \vec{F}^{q,p} \cdot \left(\delta^2 \vec{u}^p - \delta \vec{r}^{p,q} \wedge \delta \vec{\omega}^p - \vec{r}^{p,q} \wedge \delta^2 \vec{\omega}^p \right) \right) + \cdots$$
$$+ \sum_{p \in \partial V} \left(\delta \vec{F}^{\text{ext},p} \cdot \delta \vec{u}^p + \vec{F}^{\text{ext},p} \cdot \delta^2 \vec{u}^p \right) \tag{19}$$

where $\vec{r}^{p,q} = \overrightarrow{G_p C_{p,q}}$ (resp. $\vec{r}^{q,p} = \overrightarrow{G_q C_{p,q}}$) is the branch vector joining the centre G_p (resp. G_q) of particle 'p' (resp. 'q') to the contact point $C_{p,q}$ between both particles 'p' and 'q' (Fig. 10).

In these conditions, as $\vec{F}^{p,q} = -\vec{F}^{q,p}$ and $\delta \vec{F}^{p,q} = -\delta \vec{F}^{q,p}$, Eq. (12) can be expressed as:

$$W_2 = \sum_{p=1}^{N} \sum_{q=1}^{p-1} \left(\delta \vec{F}^{p,q} \cdot \delta \vec{u}_c^{p,q} + \vec{F}^{p,q} \cdot \left(\delta^2 \vec{u}^p - \delta^2 \vec{u}^q - \vec{r}^{p,q} \wedge \delta^2 \vec{\omega}^p + \vec{r}^{q,p} \wedge \delta^2 \vec{\omega}^q \right) \right) + \cdots$$
$$+ \sum_{p=1}^{N} \sum_{q=1}^{p-1} \left(\vec{F}^{p,q} \cdot \left(\delta \vec{r}^{q,p} \wedge \delta \vec{\omega}^q - \delta \vec{r}^{p,q} \wedge \delta \vec{\omega}^p \right) \right) - \sum_{p \in \partial V} \left(\vec{F}^{\text{ext},p} \cdot \delta^2 \vec{u}^p \right) \tag{20}$$
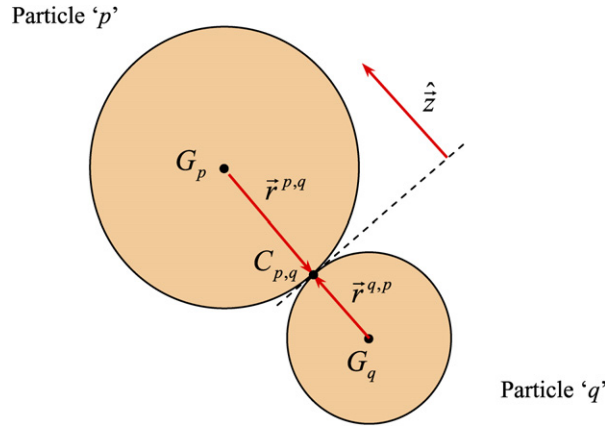
Fig. 10. Spherical particles in contact.

Fig. 10. Particules sphériques en contact.

Expression of the macroscopic second-order work in Eq. (20) introduces the quantity $\delta \vec{F}^{p,q} \cdot \delta \vec{u}_c^{p,q}$. This is not the microscopic second-order work, $W_2^{p,q} = \hat{\delta} \vec{F}^{p,q} \cdot \hat{\delta} \vec{u}_c^{p,q}$, defined on contact 'c' between particles 'p' and 'q', since $\vec{F}^{p,q}$ is differentiated with respect to $\Re$ and not to $\hat{\Re}$. However, the quantities $\delta \vec{F}^{p,q} \cdot \delta \vec{u}_c^{p,q}$ and $W_2^{p,q} = \hat{\delta} \vec{F}^{p,q} \cdot \hat{\delta} \vec{u}_c^{p,q}$ are linked by the relation (Nicot and Darve [26]):

$$W_2^{p,q} = \delta \vec{F}^{p,q} \cdot \delta \vec{u}_c^{p,q} + \left(\delta \vec{r}^{q,p} \wedge \delta \vec{\omega}^q - \delta \vec{r}^{p,q} \wedge \delta \vec{\omega}^p \right) \cdot \vec{F}^{p,q} + \cdots$$
$$+ \left(\delta^2 \vec{u}^p - \delta^2 \vec{u}^q + \vec{r}^{q,p} \wedge \delta^2 \vec{\omega}^q - \vec{r}^{p,q} \wedge \delta^2 \vec{\omega}^p \right) \cdot \vec{F}^{p,q} \tag{21}$$

By combining Eq. (20) with Eq. (21), the second-order work of the whole assembly can finally be expressed as:

$$W_2 = \sum_{p=1}^{N} \sum_{q=1}^{p-1} \left(\hat{\delta} \vec{F}^{p,q} \cdot \hat{\delta} \vec{u}_c^{p,q} \right) - \sum_{p \in \partial V} \left(\vec{F}^{\text{ext},p} \cdot \delta^2 \vec{u}^p \right) \tag{22}$$

This relation proves that the second-order work W_2 of a granular assembly is equal to the summation $\bar{W}_2 = \sum_{p=1}^{N} \sum_{q=1}^{p-1} (\hat{\delta} \vec{F}^{p,q} \cdot \hat{\delta} \vec{u}_c^{p,q})$ of the microscopic second-order works over all of the assembly's contacts, minus a complementary boundary term, $\sum_{p \in \partial V} (\vec{F}^{\text{ext},p} \cdot \delta^2 \vec{u}^p)$, which takes into account the acceleration of the particles located at the assembly's boundary. This micro–macro correspondence can be regarded as fundamental since it links a macroscopic variable, namely W_2, to micro-structural elements, namely the relative displacement and the contact force between adjoining granules. This basic relation, which bridges the 'macro-world' and the 'micro-world', provides the means to investigate a macroscopic feature, such as the unstable behaviour exhibited experimentally in Section 2, from a micro-structural point of view, as will be done in Section 5.

4. Phenomenological bifurcation analyses

In Section 2, we saw that some diffuse failure modes can occur strictly inside the Mohr–Coulomb limit surface. In Section 3, the essential meaning of negative second-order work (i.e. bursts of kinetic energy through a bifurcation point) was discussed and the link between macroscopic second-order work and microscopic discrete second-order works was established for granular media. Now it is shown that, considering incrementally piece-wise linear and nonlinear constitutive relations, it is possible to exhibit analytically and numerically bifurcation domains and cones of unstable stress directions according to the second-order work criterion.

For that we use the Eulerian expression given by Eq. (10), we assume small deformations and we neglect the changes in the geometrical configuration and obtain the classical expression:

$$W_2 = V \left(\delta \bar{\bar{\sigma}} : \bar{\bar{L}} \delta t \right) = V (\delta \bar{\bar{\sigma}} : \delta \bar{\bar{\varepsilon}}) \tag{23}$$

In addition, homogeneous specimens subjected to uniform stress–strain fields are considered for these purely material analyses.
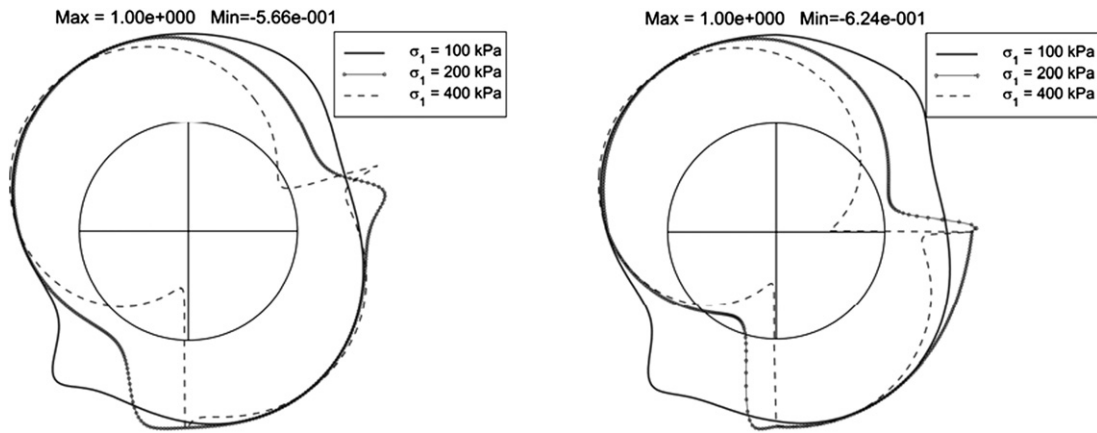
Fig. 11. Circular diagrams of the normalised second-order work $W_2/(V\|\delta\bar{\bar{\varepsilon}}\|\|\delta\bar{\bar{\sigma}}\|)$ in axisymmetric conditions ($\sigma_3 = 100$ kPa) for a dense Hostun sand—incrementally nonlinear relation (on the left) and octolinear model (on the right)—(Darve and Laouafa [8]).

Fig. 11. Représentations circulaires du travail du second ordre normalisé pour un sable d'Hostun dense en conditions axisymétriques ($\sigma_3 = 100$ kPa)—relation incrémentalement non-linéaire (à gauche) et modèle octolinéaire (à droite)—(Darve et Laouafa [8]).

Consequently, the density of second-order work W_2 appears essentially as a directional quantity:

$$W_2 = V(\delta\bar{\bar{\sigma}} : \delta\bar{\bar{\varepsilon}}) = V\big(\delta\bar{\bar{\sigma}} : \bar{\bar{\bar{M}}}(\overline{\overline{d_\sigma}})\delta\bar{\bar{\sigma}}\big) = V\big(\overline{\overline{d_\sigma}} : \bar{\bar{\bar{M}}}(\overline{\overline{d_\sigma}})\overline{\overline{d_\sigma}}\big)\|\delta\bar{\bar{\sigma}}\|^2 \tag{24}$$

with $\overline{\overline{d_\sigma}} = \delta\bar{\bar{\sigma}}/\|\delta\bar{\bar{\sigma}}\|$ and $\delta\bar{\bar{\varepsilon}} = \bar{\bar{\bar{M}}}(\overline{\overline{d_\sigma}})\delta\bar{\bar{\sigma}}$ for rate-independent materials.

To check the sign of second-order work, it is necessary to proceed—at a given stress–strain state after a given loading history—to a computation of second-order work in each stress direction. The results have been plotted in polar diagrams in stress spaces or (for more readable figures in case of negative values) in 'circular' diagrams by adding a given proper constant to the values of second-order work in order to always obtain positive values. These computations have been carried out for axisymmetric conditions (Darve and Laouafa [8]), plane strain conditions (Khoa et al. [10]) and more general 3D conditions (Darve and Laouafa [8]); in axisymmetric conditions see also Nova and Imposimato [27].

Examples of such circular diagrams are given on Fig. 11 and examples of unstable stress direction cones on Fig. 12. It appears that on the boundary of the bifurcation domain a first unstable stress direction occurs, quickly giving risen (for higher values of the deviatoric stress) to a cone of unstable stress directions, and sometimes according to the constitutive parameters to two cones.

The existence of bifurcation domains and cones of unstable stress directions for loose and dense sands were obtained with our incrementally nonlinear and piecewise linear constitutive relations. The so-called incrementally nonlinear relation of second order (INL2) is given by:

$$\delta\varepsilon_{ij} = M_{ijkl}\delta\sigma_{kl} + \frac{1}{\|\delta\bar{\bar{\sigma}}\|}M_{ijklmn}\delta\sigma_{kl}\delta\sigma_{mn} \tag{25}$$

In fixed stress–strain principal axes, it takes its simplest expression given by:

$$\begin{bmatrix} \delta\varepsilon_1 \\ \delta\varepsilon_2 \\ \delta\varepsilon_3 \end{bmatrix} = \frac{1}{2}\big[\bar{\bar{N}}^+ + \bar{\bar{N}}^-\big]\begin{bmatrix} \delta\sigma_1 \\ \delta\sigma_2 \\ \delta\sigma_3 \end{bmatrix} + \frac{1}{2\|\delta\bar{\bar{\sigma}}\|}\big[\bar{\bar{N}}^+ - \bar{\bar{N}}^-\big]\begin{bmatrix} (\delta\sigma_1) \\ (\delta\sigma_2) \\ (\delta\sigma_3) \end{bmatrix} \tag{26}$$

where the constitutive 3×3 matrices $\bar{\bar{N}}^+$ and $\bar{\bar{N}}^-$ depend on state variables and memory parameters.

The "octolinear" model corresponds to:

$$\begin{bmatrix} \delta\varepsilon_1 \\ \delta\varepsilon_2 \\ \delta\varepsilon_3 \end{bmatrix} = \frac{1}{2}\big[\bar{\bar{N}}^+ + \bar{\bar{N}}^-\big]\begin{bmatrix} \delta\sigma_1 \\ \delta\sigma_2 \\ \delta\sigma_3 \end{bmatrix} + \frac{1}{2}\big[\bar{\bar{N}}^+ - \bar{\bar{N}}^-\big]\begin{bmatrix} |\delta\sigma_1| \\ |\delta\sigma_2| \\ |\delta\sigma_3| \end{bmatrix} \tag{27}$$
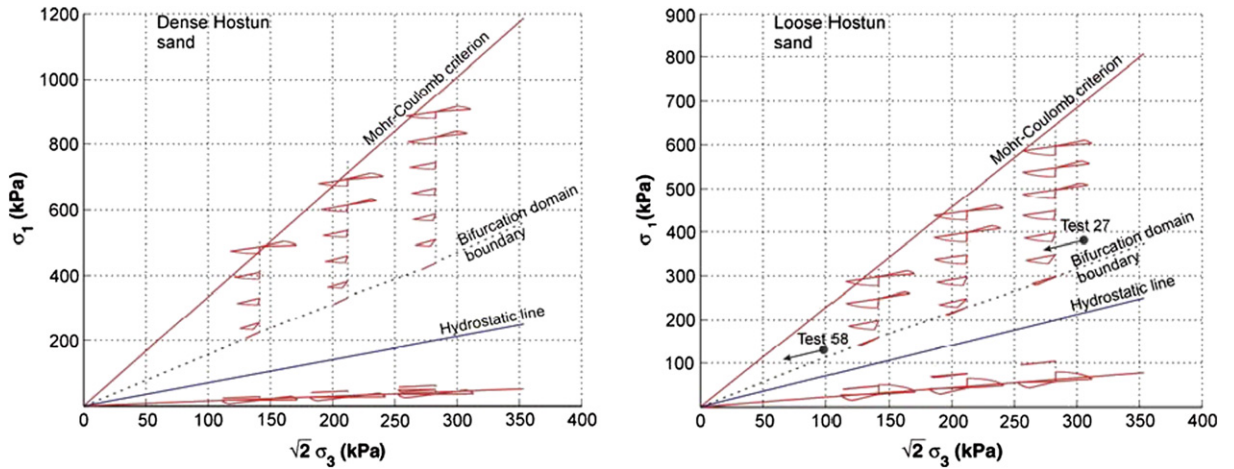
Fig. 12. Cones of unstable stress directions for dense (on the left) and loose (on the right) Hostun sand, computed with the incrementally nonlinear relation (Darve et al. [9]). The arrows in the diagram for loose sand (right) indicate the direction of stress increment at collapse for experimental tests 27 and 58 (cf. Fig. 7).

Fig. 12. Cônes de directions en contrainte instables pour un sable d'Hostun dense (à gauche) et lâche (à droite), calculés avec la relation incrémentalement non-linéaire (Darve et al. [9]). Les flèches sur la figure correspondant au sable lâche (à droite) indiquent la direction de l'incrément de contrainte lors de l'effondrement pour les essais expérimentaux 27 et 58 (cf. Fig. 7).

With this last model, the analytical determination of the bifurcation domain boundary equations and cones of unstable stress directions is made possible.

For simplicity, axisymmetric conditions and plane strain conditions are considered.

Proportional strain loading paths are used for these analyses. They are defined incrementally in axisymmetry by:

$$
\begin{cases}
\delta\varepsilon_1 = \text{constant} \\
\delta\varepsilon_2 = \delta\varepsilon_3 \text{ (axisymmetric condition)} \\
\delta\varepsilon_1 + 2R\delta\varepsilon_3 = 0 \text{ (}R\text{ constant for a given path)}
\end{cases}
\tag{28}
$$

and in plane strain by:

$$
\begin{cases}
\delta\varepsilon_1 = \text{constant} \\
\delta\varepsilon_2 = 0 \text{ (plane strain condition)} \\
\delta\varepsilon_1 + R\delta\varepsilon_3 = 0 \text{ (}R\text{ constant for a given path)}
\end{cases}
\tag{29}
$$

The second-order work takes the following forms in axisymmetry and plane strain, respectively:

$$
W_2 = V(\delta\sigma_1\delta\varepsilon_1 + 2\delta\sigma_3\delta\varepsilon_3) = V\big[(\delta\sigma_1 - \delta\sigma_3/R)\delta\varepsilon_1 + \delta\sigma_3(\delta\varepsilon_1 + 2R\delta\varepsilon_3)/R\big]
\tag{30}
$$

$$
W_2 = V(\delta\sigma_1\delta\varepsilon_1 + \delta\sigma_3\delta\varepsilon_3) = V\big[(\delta\sigma_1 - \delta\sigma_3/R)\delta\varepsilon_1 + \delta\sigma_3(\delta\varepsilon_1 + R\delta\varepsilon_3)/R\big]
\tag{31}
$$

The constitutive equation can be expressed, respectively, as:

$$
\begin{bmatrix} \delta\sigma_1 - \delta\sigma_3/R \\ \delta\varepsilon_1 + 2R\delta\varepsilon_3 \end{bmatrix} =
\begin{bmatrix} E_1^- & 2R\dfrac{E_1^- V_3^{1-}}{E_3^-} - 1 \\ 1 - 2RV_1^{3-} & \dfrac{2R^2(1 - V_3^{3-} - 2V_1^{3-}V_3^{1-})}{E_3^-} \end{bmatrix}
\begin{bmatrix} \delta\varepsilon_1 \\ \delta\sigma_3/R \end{bmatrix}
\tag{32}
$$

$$
\begin{bmatrix} \delta\sigma_1 - \delta\sigma_3/R \\ \delta\varepsilon_1 + R\delta\varepsilon_3 \end{bmatrix} =
\begin{bmatrix} \dfrac{E_1^-}{1 - V_1^{2-}V_2^{1-}} & \dfrac{E_1^-(V_3^{1-} + V_2^{1-}V_3^{2-})}{E_3^-(1 - V_1^{2-}V_2^{1-})}R - 1 \\ 1 - \dfrac{V_1^{3-} + V_1^{2-}V_2^{3-}}{1 - V_1^{2-}V_2^{1-}}R & \dfrac{DR^2}{E_3^-(1 - V_1^{2-}V_2^{1-})} \end{bmatrix}
\begin{bmatrix} \delta\varepsilon_1 \\ \delta\sigma_3/R \end{bmatrix}
\tag{33}
$$

with $D = 1 - V_1^{2-}V_2^{1-} - V_3^{3-}V_3^{1-} - V_2^{3-}V_3^{2-} - V_1^{2-}V_2^{3-}V_3^{1-} - V_2^{1-}V_1^{3-}V_3^{2-}$.

Taking into account the loading paths ($\delta\varepsilon_1 + 2R\delta\varepsilon_3 = 0$ or $\delta\varepsilon_1 + R\delta\varepsilon_3 = 0$), peaks of ($d\sigma_1 - d\sigma_3/R$) will exist (leading to negative values of second-order work according to Eqs. (30) and (31)) if and only if the determinants of the previous constitutive matrices are vanishing, giving rise to the respective bifurcation conditions:

$$2E_1^-\left(1-V_3^{3-}\right)R^2 - 2\left(E_3^- V_1^{3-} + E_1^- V_3^{1-}\right)R + E_3^- = 0 \tag{34}$$

$$E_1^-\left(1-V_2^{3-} V_3^{2-}\right)R^2 - \left[E_3^-\left(V_1^{3-}+V_1^{2-}V_2^{3-}\right) + E_1^-\left(V_3^{1-}+V_3^{2-}V_2^{1-}\right)\right]R + E_3^-\left(1-V_1^{2-}V_2^{1-}\right) = 0 \tag{35}$$

These equations have two real solutions in R if their discriminants are strictly positive.

This becomes:

$$-2(E_1^-)^2(E_3^-)^2 \det \overline{\overline{Q}}^s > 0 \tag{36}$$

$$-4(E_1^-)^2(E_3^-)^2 \det \overline{\overline{P}}^s > 0 \tag{37}$$

where $\overline{\overline{P}}^s$ and $\overline{\overline{Q}}^s$ are, respectively, the symmetric parts of the constitutive matrices given by:

$$\overline{\overline{Q}} = \begin{bmatrix} \dfrac{1}{E_1^-} & -\sqrt{2}\dfrac{V_3^{1-}}{E_3^-} \\ -\sqrt{2}\dfrac{V_1^{3-}}{E_1^-} & \dfrac{1-V_3^{3-}}{E_3^-} \end{bmatrix} \quad \text{with} \quad \begin{bmatrix} \delta\varepsilon_1 \\ \sqrt{2}\delta\varepsilon_3 \end{bmatrix} = \overline{\overline{Q}}\begin{bmatrix} \delta\sigma_1 \\ \sqrt{2}\delta\sigma_3 \end{bmatrix} \tag{38}$$

$$\overline{\overline{P}} = \begin{bmatrix} \dfrac{1-V_2^{2-}V_2^{1-}}{E_1^-} & -\dfrac{V_3^{1-}+V_3^{2-}V_2^{1-}}{E_3^-} \\ -\dfrac{V_1^{3-}+V_1^{2-}V_2^{3-}}{E_1^-} & \dfrac{1-V_2^{3-}V_3^{2-}}{E_3^-} \end{bmatrix} \quad \text{with} \quad \begin{bmatrix} \delta\varepsilon_1 \\ \delta\varepsilon_3 \end{bmatrix} = \overline{\overline{P}}\begin{bmatrix} \delta\sigma_1 \\ \delta\sigma_3 \end{bmatrix} \tag{39}$$

Thus in both cases the boundary of the bifurcation domains corresponds to the vanishing values of the determinants of the symmetric part of the constitutive matrices or, equivalently, to their first vanishing eigen-values. However, for such incrementally piecewise linear constitutive relations, it is necessary to check whether the unstable stress directions are indeed inside the tensorial zone chosen at the beginning of the calculation (and given here by the indices + and −). This condition has been checked numerically and verified.

The first unstable directions correspond to the double root of Eqs. (35) and (36) exactly for nil discriminants.

The eigen-vectors associated with the vanishing eigen-values are given by:

$$E_1^- \delta\varepsilon_1 + \left(2\frac{E_1^-}{E_3^-}V_3^{1-} - \frac{1}{R}\right)\delta\sigma_3 = 0 \tag{40}$$

$$E_1^- \delta\varepsilon_1 + \left(\frac{E_1^-}{E_3^-}(V_3^{1-} + V_3^{2-}V_2^{1-}) - \frac{1}{R}\right)\delta\sigma_3 = 0 \tag{41}$$

and characterise the bifurcation/collapse mechanism (Darve et al. [9], Khoa et al. [10]).

5. Numerical bifurcation analyses

Diffuse failure modes strictly inside the Mohr–Coulomb limit surface have been exhibited experimentally in Section 2, a bifurcation criterion (the sign of second-order work) was proposed in Section 3 and was applied in Section 4 in a phenomenological context to determine the bifurcation domains and cones of unstable stress directions. In this fifth section, the bifurcation criterion is considered in a numerical discrete context. The macro–micro correspondence between the second-order work and micro-structural variables demonstrated in Section 3.3 is discussed. Then it is shown that the occurrence of loss of sustainability corresponds to the vanishing of the second-order work.

5.1. The discrete numerical model

The numerical simulations were carried out with the 3D software SDEC (Magnier and Donzé [13]) based on the discrete element method as proposed by Cundall and Strack [28] to describe the mechanical behaviour of granular soils. Grains are rigid spheres of diameter D_s. The intergranular interaction is simulated in the direction normal to the contact by a linear elasticity with a stiffness $k_n/D_s = 356$ MPa, and in the tangential direction by a linear elasticity $(k_t/k_n = 0.42)$ and a tangential perfect plasticity with a friction angle $\varphi = 35°$. The normal and the tangential contact forces, F_n and F_t, respectively, are given by:

$$\begin{Bmatrix} F_n = k_n \delta_n \\ F_n > 0 \end{Bmatrix} \qquad \begin{Bmatrix} \Delta F_t = k_t \Delta u_t \\ F_t \leqslant \tan\varphi F_n \end{Bmatrix} \tag{42}$$

where δ_n is the overlap at the contact point and Δu_t is the incremental tangential displacement. At the beginning of a computational time-step, contact forces are computed from sphere positions and then resultant forces and momentums on each sphere. Finally new sphere positions are calculated by applying Newton's second law. The integration in time of Newton's second law and the interaction contact law are both carried out by way of an explicit scheme.

The numerical specimen of volume V has a cubical shape and is composed of roughly 10 000 spheres whose size distribution is continuous (2 mm $\leqslant D_s \leqslant$ 9.5 mm). The loading path (strain, stress or mixed control parameters) is imposed on the sphere assembly by controlling the positions of six frictionless walls in contact with spheres at the boundaries of the specimen. In this paper, simulations are limited to axisymmetric stress–strain states ($\sigma_2 = \sigma_3$ and $\varepsilon_2 = \varepsilon_3$).

5.2. Computation of macro- and micro-values of second-order work

Axisymmetric stress probes were performed to compute the semi-Lagrangian (Eq. (7)) and the Eulerian (Eq. (10)) expressions of the macroscopic second-order work. Stress probes are performed from an initial stress–strain state by imposing a loading vector $\delta\vec{\sigma}$ defined in the Rendulic plane of stress increments ($\delta\sigma_1$, $\sqrt{2}\delta\sigma_3$) by its norm $\|\delta\vec{\sigma}\| = 1$ kPa and the angle α between the $\sqrt{2}\delta\sigma_3$ axis and $\delta\vec{\sigma}$ (see Fig. 13(a)). α is increased from 0° to 360° by increments of 10° to check each stress direction. The corresponding response vectors $\delta\vec{\varepsilon}$, defined in the Rendulic plane of strain increments ($\delta\varepsilon_1$, $\sqrt{2}\delta\varepsilon_3$) (Fig. 13(b)) are computed. The initial stress–strain state of stress probes results from an isotropic compression up to 200 kPa followed by an axisymmetric triaxial compression ($\sigma_2 = \sigma_3 = $ cst.) stopped at $\eta = \frac{\sigma_1-\sigma_3}{(\sigma_1+2\sigma_3)/3} = 0.77$.

Fig. 14(a) shows the density of second-order work (i.e. the second-order work per unit of volume) through the semi-Lagrangian formalism, the Eulerian formalism and its three components $\delta\overline{\overline{\sigma}} : \overline{\overline{L}}\delta t$, $\mathrm{div}(\delta\vec{u})\overline{\overline{\sigma}} : \overline{\overline{L}}\delta t$, $\overline{\overline{\sigma}}(\overline{\overline{L}})^t\delta t : \overline{\overline{L}}\delta t$ versus the stress-probe direction α. Note that values of the second-order work are higher in the central part of the diagram because (as explained below) stress probes in these directions (i.e. $50° < \alpha < 260°$) lead to irreversible strains larger than reversible strains found along the other directions. The most important contributing term in the Eulerian expression of W_2 is $\delta\overline{\overline{\sigma}} : \overline{\overline{L}}\delta t$. Then the term $\mathrm{div}(\delta\vec{u})\overline{\overline{\sigma}} : \overline{\overline{L}}\delta t$, which takes into account the volumetric strain through the factor $\mathrm{div}(\delta\vec{u})$, is nearly nil whatever the stress-probe direction. Finally, the term $\overline{\overline{\sigma}}(\overline{\overline{L}})^t\delta t : \overline{\overline{L}}\delta t$ is small but not inconsiderable for stress probes leading to irreversible strains. Nicot and Darve [26] showed that this latter term can be linked to the change in the fabric of the granular assembly. The reference state to compute the semi-Lagrangian expression of W_2 is the initial state before stress probes. These semi-Lagrangian and Eulerian expressions of second-order work are shown to be equivalent, as expected from analytical developments (Section 3.2). The expression $\delta\overline{\overline{\sigma}} : \overline{\overline{L}}\delta t$, often used to compute the density of second-order work, misestimates the expression originally given by Hill [11], Eq. (7), when strains are large.

The cones of unstable stress directions and the bifurcation domain computed with the discrete numerical model are presented in Sibille et al. [29] and compared with those found with the INL2 and a micro-mechanical model.

In Fig. 14(b), the macroscopic density of second-order work (semi-Lagrangian or Eulerian expression) and the expression $\frac{1}{V}\sum_{p=1}^{N}\sum_{q=1}^{p-1}(\delta\vec{F}^{p,q} \cdot \delta\vec{u}_c^{p,q})$, which is the density of the microscopic second-order work $\bar{W}_2$, are compared. For $\alpha \leqslant 70°$ and $\alpha \geqslant 230°$ macro- and micro-values of second-order work are numerically equal, whereas it is
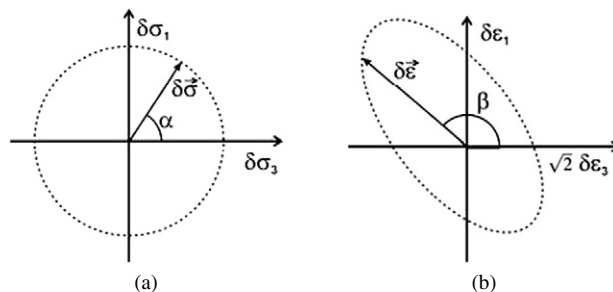

Fig. 13. Definition of Rendulic planes; (a) stress probes and (b) strain responses.

Fig. 13. Définition des plans de Rendulic : recherches directionnelles en contrainte (a) et réponses en déformation (b).
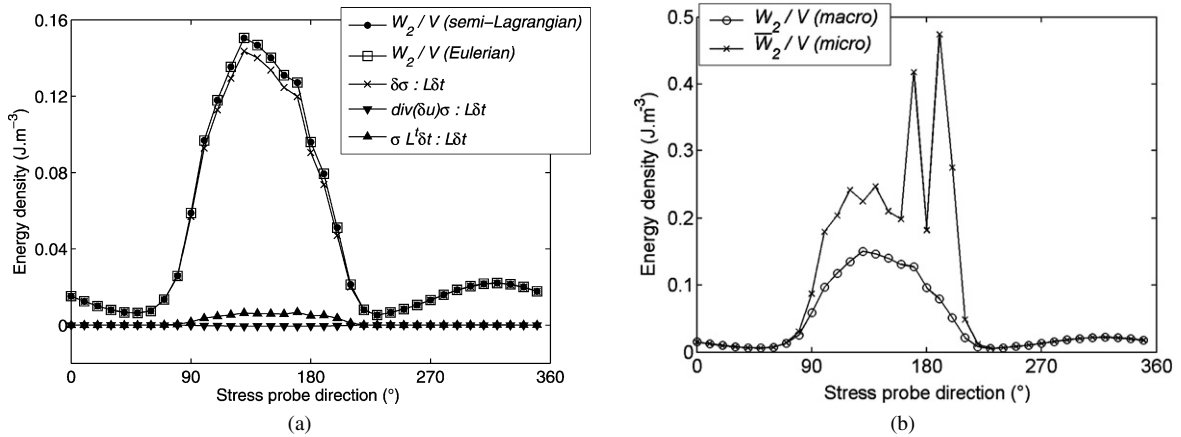
Fig. 14. Density of second-order work; (a) macroscopic and (b) microscopic expression.

Fig. 14. Densité de travail du second ordre ; expressions macroscopique (a) et microscopique (b).
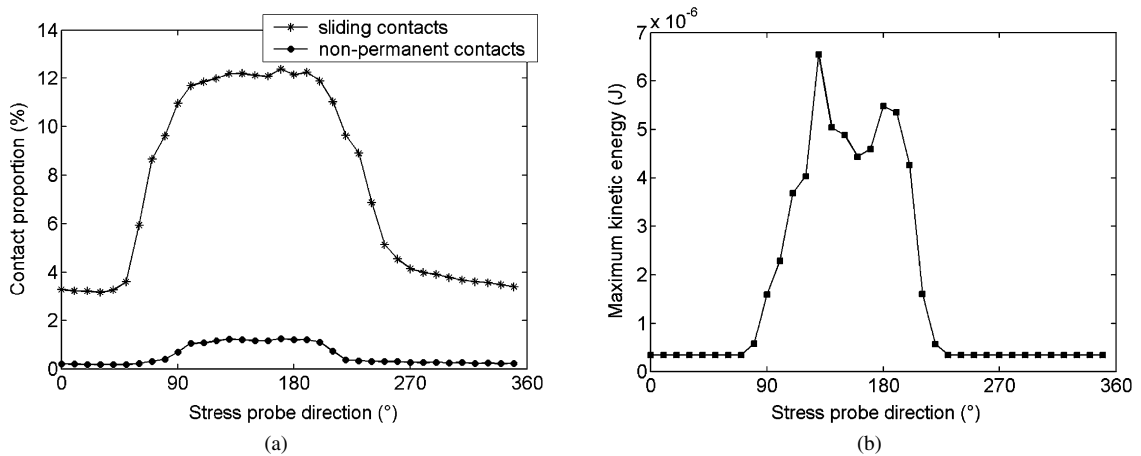

Fig. 15. (a) Percentage of sliding and nonpermanent contacts; (b) maximum kinetic energy.

Fig. 15. Pourcentage de contacts glissants et non-permanents (a) ; maximums d'énergie cinétique (b).

no longer true for $70° < \alpha < 230°$. Let us note that the complementary term $\sum_{p \in \partial V}(\vec{F}^{\text{ext},p} \cdot \delta^2 \vec{u}^p)$ of Eq. (22) has not been taken into account even though accelerations of spheres at the boundaries of the specimen are not necessarily nil for stress probes. On the contrary, by performing strain probes, sphere velocity at the boundaries can nearly be maintained at a constant value; making the complementary term vanish. However, the gap between macro- and micro-values of the second-order work is not modified. Therefore, we consider that the weight of the complementary term is negligible for the simulations presented in this paper, whatever the control mode (constant stress or constant strain rate).

Fig. 15(a) shows the percentage, with respect to the initial number of contacts, of nonpermanent contacts (i.e. contacts which do not persist during the simulation) and contacts that reached Coulomb criterion at least during one time-step (sliding contacts), versus the stress-probe direction α. We call the interval $50° < \alpha < 260°$ the irreversible strain range since the proportion of nonpermanent and sliding contacts is high compared to the complementary interval, called the reversible strain range (even if it is not totally true since the number of sliding and nonpermanent contacts is not strictly nil). Stress probe directions exist inside the irreversible range such that macro- and micro-values of the second-order work are equal ($\alpha = 60°$; $70°$; $230°$; $240°$; $250°$); thus the difference found between both expressions of second-order work is not directly related to the fact that some contacts slide, open or create. Fig. 15(b) shows, for each stress-probe direction, the maximum value of kinetic energy found during the simulation. The interval for which the kinetic energy is not negligible ($70° < \alpha < 230°$) is included inside the irreversible range. Irreversible

strains can therefore be related to both quasi-static and dynamic regimes. Macro- and micro-values of the second-order work are no longer equal as soon as dynamic irreversible strains, accompanied by substantial micro-structural rearrangements, exist. We conclude that the micro–macro correspondence (Eq. (22)) is numerically verified for quasi-static reversible or irreversible strains.

The disagreement found for dynamic irreversible strains can be explained by the fact that the second-order work is an impulsive value valid at initial time t corresponding to an equilibrium state. From a numerical point of view, the second-order work is computed over a finite time increment between an initial and a final state. When dynamic events appear, the strain or the stress path (depending on the loading mode) is strongly nonlinear and rate terms appearing in the definition of the second-order work cannot be assessed from finite increments as used in any experimental or numerical tests. Consequently, the computation of the microscopic second-order work between the initial and final states is no longer valid when local dynamic events occur.

5.3. Simulation of diffuse failure modes

Hereafter simulations are presented of diffuse failure modes for axisymmetric proportional strain paths defined in Section 4 by Eq. (28). For $R = 1$, the path is characterised by isochoric strain, for $0 < R < 1$ it is dilatant, while for $R > 1$ it is contractant.

The conjugate variables with respect to energy are $\sigma_1 - \sigma_3/R$ versus ε_1 and $\varepsilon_1 + 2R\varepsilon_3$ versus σ_3/R, thus the second-order work (by assuming small deformations and by neglecting the changes in the geometrical configuration) is taking the form of Eq. (30). The control parameters are $\varepsilon_1 + 2R\varepsilon_3$ and ε_1 or $\varepsilon_1 + 2R\varepsilon_3$ and $\sigma_1 - \sigma_3/R$. In Fig. 16(a) and 16(b) the proportional strain paths simulated are shown, after an isotropic compression up to 100 kPa, by imposing the control parameter $\delta\varepsilon_1 > 0$ and for different values of R. For R values lower than 0.85, $\sigma_1 - \sigma_3/R$ possesses a maximum (Fig. 16(b)). The second term of Eq. (30) is nil so that the second-order work vanishes at the peak value of $\sigma_1 - \sigma_3/R$ and thereafter takes negative values. Loss of sustainability of the numerical sample may therefore occur from the peak of $\sigma_1 - \sigma_3/R$ and along the descending branch.

For $R = 0.825$ two equilibrium states denoted ES_a and ES_b in Fig. 16(b) are considered and the control parameters chosen are $(\delta\varepsilon_1 + 2R\delta\varepsilon_3)/R = 0$ (proportional strain path) and $\delta\sigma_1 - \delta\sigma_3/R$. If $\delta\sigma_1 - \delta\sigma_3/R = 0$ is strictly imposed, both equilibrium states ES_a and ES_b do not evolve. Then ES_a and ES_b are perturbed by an infinitesimally small perturbation, namely a positive value of $\delta\sigma_1 - \delta\sigma_3/R$ that is very small with respect to the stress states at ES_a and ES_b. For the state ES_a, we choose $\delta\sigma_1 - \delta\sigma_3/R = 500$ Pa, which represents 2% of $\sigma_1 - \sigma_3/R$ at ES_a. Let us denote $\chi = (\sigma_1 - \sigma_3/R)_t/(\sigma_1 - \sigma_3/R)_{t=0}$, where t is the simulation numerical time. χ and kinetic energy K versus t are shown in Fig. 17(a). The numerical specimen reaches a novel stress state (a little bit higher in the figure than the previous one) and the values of kinetic energy remain very low: a novel equilibrium state is attained. For ES_b, $\delta\sigma_1 - \delta\sigma_3/R = 250$ Pa (half the perturbation imposed at ES_a), which represents 1% of $\sigma_1 - \sigma_3/R$ at ES_b. Results
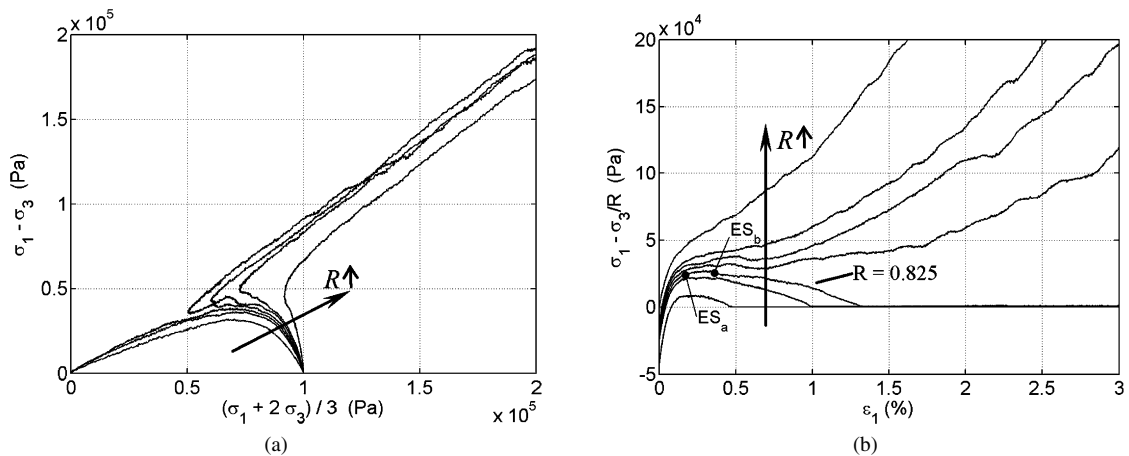

Fig. 16. Proportional strain paths for $R = 0.7$; 0.8; 0.825; 0.85; 0.875; 0.9; 1.0.

Fig. 16. Chemins proportionnels en déformation pour $R = 0,7$; 0,8; 0,825; 0,85; 0,875; 0,9; 1,0.
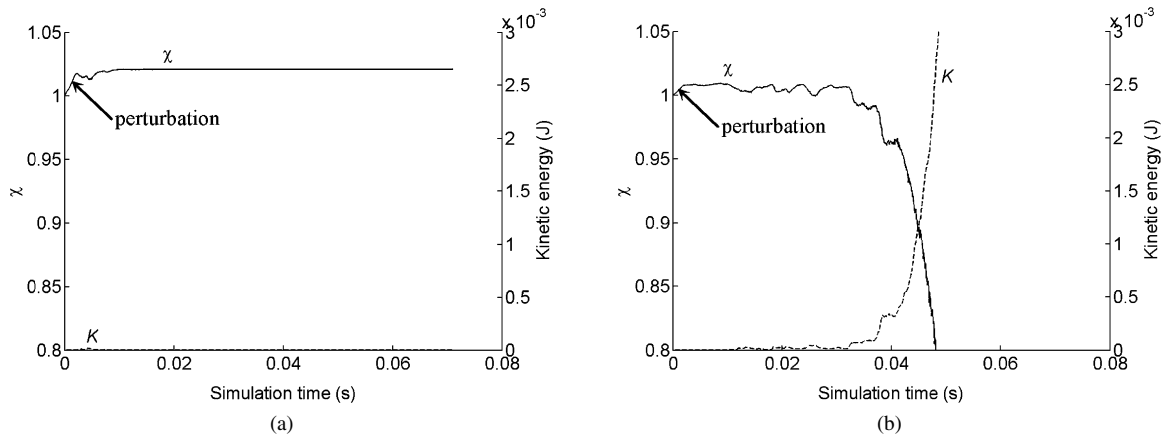
Fig. 17. Perturbation in $\sigma_1 - \sigma_3/R$: stress state and kinetic energy changing from equilibrium state ES_a (a) and ES_b (b).

Fig. 17. Perturbation en : évolution de l'état de contrainte et de l'énergie cinétique à partir des états d'équilibre ES_a (a) et ES_b (b).
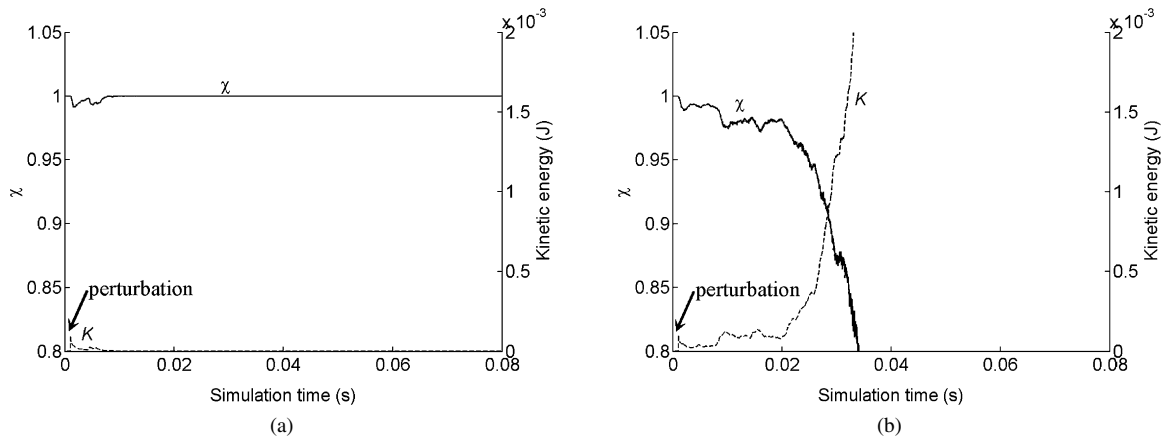

Fig. 18. Perturbation in kinetic energy: stress state and kinetic energy changing from equilibrium state ES_a (a) and ES_b (b).

Fig. 18. Perturbation en énergie cinétique : évolution de l'état de contrainte et de l'énergie cinétique à partir des états d'équilibre ES_a (a) et ES_a (b).

are shown in Fig. 17(b). In contrast to the previous case, the stress state does not reach the imposed value and finally dramatically decreases at a high rate, while the kinetic energy increases exponentially: the numerical specimen totally collapses (the equilibrium state of the specimen is not sustainable).

In the simulations presented above, equilibrium states are perturbed by the control parameters being perturbed. However, in experimental tests, many sources of perturbation exist. We present in the following another way of perturbing the equilibrium states.

The control parameter $\sigma_1 - \sigma_3/R$ is maintained constant. Since gravity is not taken into account, some spheres, included in the specimen, float at a given equilibrium state and they are not involved (for this state) in the contact force network. Some of these spheres, chosen randomly, are perturbed by imposing a given instantaneous velocity in a random direction. The perturbation therefore corresponds to an external input of kinetic energy.

Equilibrium states ES_a and ES_b are perturbed by injecting 1×10^{-4} J to the numerical specimen. By comparison, the maximum value of kinetic energy for the proportional strain paths (Fig. 16(b)) is approximately 1×10^{-3} J. Results for ES_a and ES_b are shown in Fig. 18(a) and 18(b), respectively. The responses are similar to the ones found by perturbing $\sigma_1 - \sigma_3/R$, from state ES_a a new equilibrium is reached (the kinetic energy, after some burst vanishes), whereas from state ES_b the total collapse of the specimen is observed.

We showed here that for proper control parameters and for bifurcation points detected by the second-order work criterion, a 'small perturbation' of one of the control parameters or of the energy state of the system can cause a strong

discontinuous change in the mechanical response of the system (i.e. the occurrence of a sudden diffuse failure mode) under constant control parameters.

6. Conclusion

In the second section of this paper, failure states were exhibited experimentally, which cannot be described by a Mohr–Coulomb plastic limit condition or a strain localisation criterion. These collapses seem to have a diffuse nature after these experiments, among others.

The next section presented the second-order work (W2) criterion as a possible candidate to describe these collapses. Eulerian and semi-Lagrangian expressions of W2 were established and it was proven that the existence of negative values of W2 is related to bursts of kinetic energy. Thus the corresponding mechanical states of the material cannot be sustained; a bifurcation point has been reached. Then the relation between the macroscopic second-order work and the sum of the local discrete second-order works in granular media shows how the macroscopic instabilities are closely related to local intergranular instabilities.

In Section 4, the second-order work criterion applied in a phenomenological context allowed us to analytically determine and numerically verify the boundaries of the bifurcation domains and the unstable stress direction cone equations.

Finally in the last section, using a discrete element numerical model, we checked and validated the relations established in Section 3, to compare macro- and microscopic values of second-order work and to simulate numerically diffuse failure modes exactly under the conditions predicted in Section 4.

In other papers (Nicot and Darve [30,31]), these questions were also explored by considering a micro-mechanical model. As a last remark, let us conclude that all these analyses lead to a generalised vision of failure in civil engineering by taking into account failure modes that have not been considered until now. Applications to landslides, rockfalls and snow avalanches are in progress in European projects and national ANR projects.

References

[1] J. Boussinesq, Application des potentiels à l'étude de l'équilibre et du mouvement des solides élastiques, Gauthier-Villars, Paris, 1885.
[2] F. Darve, Effet des surcharges rectangulaires à distances et à profondeurs variables sur un mur vertical, projet de fin d'études, CEBTP, Ecole Centrale, Paris, 1971.
[3] J. Boussinesq, Essai théorique sur l'équilibre des massifs pulvérulents et sur la poussée des terres sans cohésion, Académie Royale de Belgique, Bruxelles, 1876.
[4] F. Darve, X. Roguiez, Homogeneous bifurcation in soils, in: Adachi, et al. (Eds.), Localization and Bifurcation Theory for Soils and Rocks, Balkema, 1998, pp. 43–50.
[5] J.R. Rice, The localization of plastic deformation, in: W.T. Koiter (Ed.), Theoretical and Applied Mechanics, North-Holland Publishing Company, Delft, 1976, pp. 207–220.
[6] F. Darve, B. Chau, Constitutive instabilities in incrementally non-linear modelling, in: C.S. Desai (Ed.), Constitutive Laws for Engineering Materials, 1987, pp. 301–310.
[7] R. Nova, Liquefaction, stability, bifurcations of soil via strain-hardening plasticity, in: E. Dembicki, et al. (Eds.), Numerical Methods for Localisations and Bifurcations of Granular Bodies, Tech. Univ. of Gdansk Publ., 1989, pp. 117–132.
[8] F. Darve, F. Laouafa, Instabilities in granular materials and application to landslides, Mech. Cohes. Frict. Mater. 5 (8) (2000) 627–652.
[9] F. Darve, G. Servant, F. Laouafa, H.D.V. Khoa, Failure in geomaterials: continuous and discrete analyses, Computer Meth. Appl. Mech. Eng. 193 (27–29) (2004) 3057–3085.
[10] H.D.V. Khoa, I.O. Georgopoulos, F. Darve, F. Laouafa, Diffuse failure in geomaterials: Experiments and modelling, Computers and Geotechnics 33 (2006) 1–14.
[11] R. Hill, A general theory of uniqueness and stability in elastic–plastic solids, J. Mech. Phys. Solids 6 (1958) 236–249.
[12] J. Mandel, Conditions de stabilité et postulat de Drucker, in: J. Kravtchenko, P.M. Sirieys (Eds.), Rheology and Soil Mechanics, Springer, 1964, pp. 58–68.
[13] S.A. Magnier, F.V. Donzé, Numerical simulations of impacts using a discrete element method, Mech. Cohes. Frict. Mater. 3 (1998) 257–276.

[14] J.D. Eckersley, Instrumented laboratory flowslides, Géotechnique 40 (3) (1990) 489–502.

[15] P. Skopek, N.R. Morgenstern, P.K. Robertson, D.C. Sego, Collapse of dry sand, Can. Geotech. J. 31 (1994) 1008–1014.

[16] S. Sasitharan, P.K. Robertson, D.C. Sego, N.R. Morgenstern, Collapse behavior of sand, Can. Geotech. J. 30 (1993) 569–577.

[17] C. di Prisco, S. Imposimato, Experimental analysis and theoretical interpretation of triaxial load controlled loose sand specimen collapses, Mech. Cohes. Frict. Mater. 2 (1997) 93–120.

[18] A. Gajo, The influence of system compliance on collapse of triaxial sand samples, Can. Geotech. J. 41 (2004) 257–273.

[19] R. Matiotti, C. di Prisco, R. Nova, Experimental observations on static liquefaction of loose sand, in: K. Ishihara (Ed.), Earthquake Geotechnical Engineering, Balkema, 1995, pp. 817–822.

[20] T. Doanh, E. Ibraim, R. Matiotti, Undrained instability of very loose Hostun sand in triaxial compression and extension. Part 1: experimental observations, Mech. Cohes. Frict. Mater. 2 (1997) 47–70.

[21] G. Servant, F. Darve, J. Desrues, I.O. Georgopoulos, Diffuse modes of failure in geomaterials, in: H. Di Benedetto, et al. (Eds.), Deformation Characteristics of Geomaterials, Taylor & Francis Group, 2005, pp. 181–200.

[22] R. Nova, Controllability of the incremental response of soil specimens subjected to arbitrary loading programmes, J. Mech. Behav. Mater. 5 (2) (1994) 193–201.

[23] S. Imposimato, R. Nova, Instabilities of loose sand specimens in undrained tests, in: T. Adachi, F. Oka, A. Yashima (Eds.), Localisation and Bifurcation Theory for Soils and Rocks, Balkema, 1998, pp. 313–322.

[24] H. Petryk, Theory of bifurcation and instability in time-independent plasticity, in: Q.S. Nguyen (Ed.), Bifurcation and Stability of Dissipative Systems, in: CISM Courses and Lectures, vol. 327, Springer, 1993, pp. 95–152.

[25] D. Bigoni, Bifurcation and instability of non-associative elastoplastic solids, in: H. Petryk (Ed.), Material Instabilities in Elastic and Plastic Solids, in: CISM Courses and Lectures, vol. 414, Springer-Verlag, 2000, pp. 1–52.

[26] F. Nicot, F. Darve, A micro-mechanical investigation of bifurcation in granular materials, Int. J. Solids Structures 44 (2007) 6630–6652.

[27] R. Nova, S. Imposimato, Non-uniqueness of the incremental response of soil specimens under true-triaxial stress paths, in: G. Pande, S. Pietruszczak (Eds.), NUMOG VI, Balkema, 1997, pp. 193–197.

[28] P.A. Cundall, O.D.L. Strack, A discrete numerical model for granular assemblies, Géotechnique 29 (1) (1979) 47–65.

[29] L. Sibille, F. Nicot, F.V. Donzé, F. Darve, Material instability in granular assemblies from fundamentally different models, Int. J. Numer. Anal. Meth. Geomech. 31 (2007) 457–481.

[30] F. Nicot, F. Darve, A multi-scale approach to granular materials, Mech. Mat. 37 (2005) 980–1006.

[31] F. Nicot, F. Darve, Micro-mechanical investigation of material instability in granular assemblies, Int. J. Solids Structures 43 (2006) 3569–3595.